ELSEVIER

Journal of Fluids and Structures 26 (2010) 393–405

JOURNAL OF FLUIDS AND STRUCTURES

www.elsevier.com/locate/jfs

Shear flow over cylindrical rods attached to a substrate

C. Pozrikidis

Department of Chemical Engineering, University of Massachusetts, Amherst, MA 01003, USA

Received 10 July 2009; accepted 21 January 2010

Abstract

Shear flow over a periodic array of cylindrical rods attached to a substrate is studied as a model of flow over a nanomat consisting of aligned carbon nanotubes. The objectives are to evaluate the macroscopic slip velocity, compute the hydrodynamic load exerted at the rod side surface and tip, and estimate the flow-induced deflection. The hydrodynamic traction and macroscopic slip velocity are computed by solving the equations of Stokes flow for a doubly periodic square or hexagonal arrangement using a boundary-element method. The results illustrate the dependence of the slip velocity on the surface coverage expressed by the ratio of the rod radius to separation, and confirm the occurrence of hydrodynamic screening due to surrounding rods confining the traction near the exposed tip of each rod. An estimate for the flexural stiffness of nanotubes is made using available information on the flow-induced deflection. Computations for shear flow past an isolated attached rod are carried out using a highly accurate boundary-element method coupled with a finite-element method for solving the Euler–Bernoulli beam equation, and an iterative procedure involving a boundary-element implementation coupled with a boundary-value formulation involving ordinary differential equations for describing large beam deformation. The results illustrate the precise shape of deflected rods.

Keywords: Shear flow; Elastic rods; Nanomat; Nanotubes; Beam deflection

1. Introduction

Dense arrays of parallel carbon nanotubes can be grown on substrates using thermal chemical vapor deposition (CVD) and other techniques, yielding surfaces that resemble nanomats, nanocarpets, or nanoforests [e.g., Deck and Vecchio (2005), Xu et al. (2006)]. Ni et al. (2008) demonstrated that measuring the deflection of the individual nanotubes due to an overpassing flow can be used to deduce the flexural rigidity of the rolled hexagonal atomic lattice comprising the nanotubes. In their experiments, the nanotube deflection was inferred from the attenuation of a laser sheet transmitted through a sample. Classical Euler–Bernoulli beam theory combined with data fitting was then applied to evaluate the flexural rigidity. Further interest in flow over nanomats and other patterned surfaces is motivated by the desire to reduce the hydrodynamic surface drag coefficient and effective contact angle at a three-phase contact angle, most likely due to the entrapment of gas. Motivated by this possibility, Ford and Papavassiliou (2006) computed shear flow past a single file and a doubly periodic hexagonal array of nanotubes attached to a substrate and provided data illustrating the effect of fluid inertia.

In the first part of this paper, a theoretical model of an idealized nanomat comprised of a doubly periodic array of semi-infinite cylindrical rods is developed. Because shear flow over the nanomat decays rapidly with distance into the

E-mail address: cpozrikidis@ecs.umass.edu

0889-9746/$ - see front matter © 2010 Elsevier Ltd. All rights reserved.
doi:10.1016/j.jfluidstructs.2010.01.008

tight space between the rods, the presence of a support can be neglected as a first approximation. The objectives are to evaluate the macroscopic slip velocity due to the fibrous nanomat constitution and provide an estimate for the nanotube deflection for small deformation. The former is possible thanks to a special implementation of the boundary-element method that employs the doubly periodic Green's function of Stokes flow computed in terms of Ewald sums. We find that, for dense arrangements, the exposed tips of the rods receive the majority of the hydrodynamic load due to the shear flow. Reliable estimates for the rod deformation may then be obtained and the flexural stiffness can be estimated using the Euler–Bernoulli beam theory for a cantilever with a concentrated tip load.

In the second part of this paper, we consider shear flow over a single isolated rod attached to an infinite plane with the objective of precisely describing the flow-induced deformation. The axially symmetric shape of the undeformed rod allows us to apply Fourier expansions with respect to the meridional angle measured around the rod axis, and thereby accurately evaluate the hydrodynamic load applied at the tip of the rod and along the cylindrical surface. By integrating the hydrodynamic traction over the circular rod contour in a horizontal plane, we obtain an effective load density along the centerline. By integrating the hydrodynamic traction over the exposed top surface of the rod, we obtain a concentrated tip load accompanied by a bending moment. Once these results are available, the small deflection of rods with arbitrary length to radius ratio is computed by solving the Euler–Bernoulli equation for an elastic beam using a finite-element method. The numerical predictions are compared with analytical results for a cantilever supporting a tip or distributed load, and significant differences are identified.

In the third part of this paper, the restriction of small deflection imposed in Section 2 is relaxed and an iterative procedure is implemented for computing significantly deformed shapes of an isolated rod. The approach involves assuming a deflected rod shape, computing hydrodynamic boundary-element tractions by solving an integral equation over the rod surface, projecting the traction to the centerline, solving a boundary-value problem involving ordinary-differential equations for the centerline shape, and then reconstructing a new rod shape by interpolation. The procedure is repeated until convergence. The numerical results will be shown to be in excellent agreement with the small-deformation analysis presented in Section 2. The significance of the analysis to biological systems is discussed in the Conclusion.

2. Flow over a doubly periodic array

Photographs of nanomats consisting of an array of carbon nanotubes attached to a substrate and deforming under the action of an overpassing flow were presented by Ni et al. (2008). In our theoretical model, the nanomat is idealized as a doubly periodic array of parallel rods. Cartesian coordinates are introduced with the x and y axes parallel to the nanomat and the z axis parallel to the undeformed rods, as shown in Fig. 1. The origin of the z axis is set at the aligned tips of the microarray. We will consider nanotubes arranged on a square lattice with base vectors $\mathbf{a}_1 = (L,0)$ and $\mathbf{a}_2 = (0,L)$, and nanotubes arranged on a hexagonal lattice with base vectors $\mathbf{a}_1 = (L,0)$ and $\mathbf{a}_2 = (L/2, \sqrt{3}L/2)$, where L is the shortest distance between two nanotube centerlines.

Far above the array, as $z \to \infty$, the fluid velocity, $\mathbf{u}$, obtains a linear distribution expressing simple shear flow,

$$\mathbf{u} \simeq \xi z \mathbf{e} + \mathbf{U}_s + \cdots \tag{1}$$

where ξ is the shear rate, $\mathbf{e}$ is a unit vector tangential to the xy plane, $\mathbf{U}_s$ is an *a priori* unknown slip velocity parallel to the xy plane, and the dots represent exponentially decaying terms. For densely populated arrays and long nanotubes, the velocity decays exponentially with distance from the tips inside the array. Since the fluid becomes virtually quiescent at the lower end of the array, the presence of the substrate can be neglected as a first approximation.

At low Reynolds numbers, the motion of the fluid is governed by the Stokes equation and the continuity equation, [e.g., Pozrikidis (1992)]. The fluid velocity is assumed to satisfy the no-slip and no-penetration boundary condition demanding zero velocity over the top and cylindrical surface of each rod. The conditions for the Stokes equation and slip boundary condition to be valid are discussed by Ford and Papavassiliou (2006). In our computations, we seek to describe the velocity field and evaluate the slip velocity for specified nanomat geometry, shear rate, ξ, and direction of the shear flow parallel to the xy plane.

2.1. Boundary-element solution

An efficient boundary-integral formulation for computing doubly periodic Stokes flow was developed in earlier work (Pozrikidis, 2001). The integral formulation relies on the Greens function describing the doubly periodic flow due to a two-dimensional lattice of three-dimensional point forces deployed parallel to the xy plane whose geometry coincides

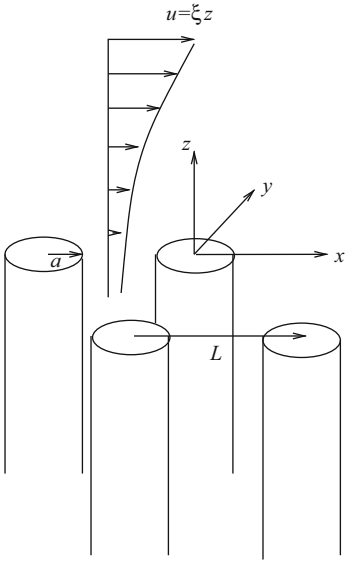

Fig. 1. Illustration of shear flow over a doubly periodic array of semi-infinite cylinders of radius a and separation L modeling a nanomat.

with that of the nanotube array. The velocity field induced by the point forces at a point $\mathbf{x}$ is given by

$$u_i(\mathbf{x}) = \frac{1}{8\pi\mu} G_{ij}(\mathbf{x},\mathbf{x}_0) b_j, \tag{2}$$

where μ is the fluid viscosity, $\mathbf{G}$ is the velocity Greens function tensor, and $\mathbf{b}$ is the strength of each point force. One arbitrarily selected point force is located at the point $\mathbf{x}_0$. Far above the point force array, as the difference $z-z_0 \to \infty$,

$$G_{ij}(\mathbf{x},\mathbf{x}_0) \simeq \frac{8\pi}{A}(z-z_0) J_{ij} + \cdots, \tag{3}$$

where A is the area of a unit cell in the xy plane and $\mathbf{J}$ is the identity matrix except that the third diagonal component corresponding to the z axis is set to zero. Far below the point force array, as $z-z_0 \to -\infty$, the Green's function decays exponentially with shifted distance, $z-z_0$. The efficiency of the numerical method hinges on the expedited computation of the Green's function using Ewald sums (Pozrikidis, 1996).

The boundary-integral equation provides us with an integral representation for the velocity field,

$$u_j(\mathbf{x}_0) = -\frac{1}{8\pi\mu} \iint G_{ij}(\mathbf{x},\mathbf{x}_0) f_i(\mathbf{x}) \, \mathrm{d}S(\mathbf{x}) + \xi z_0 e_j + U_{s_j}, \tag{4}$$

where $\mathbf{f}$ is the hydrodynamic traction and the surface integral is computed over one cylinder surface. A companion condition specifies that the force exerted on each cylinder balances the drag force imparted to the cylinder by the shear flow,

$$\iint \mathbf{f}(\mathbf{x}) \, \mathrm{d}S(\mathbf{x}) = \mu\xi A \mathbf{e}. \tag{5}$$

Enforcing the integral representation (4) at the surface of a cylinder and requiring the condition of zero velocity we obtain an integral equation for the hydrodynamic traction.

To solve the integral equation, we divide the top and side surface of one chosen cylinder into six-node flat or curved boundary elements and approximate the Cartesian components of the traction with constant functions over each element. The boundary-element discretization is carried out using a custom-made algorithm based on the successive subdivision of a four- or eight-element pattern. The side surface arises by rolling a discretized square into a cylinder of radius a and length $d = 2\pi a$. Enforcing the integral equation at collocation points located at the boundary element centroids, we obtain a system of linear algebraic equations for the Cartesian components of the element traction. The slip velocity arises directly as part of the solution by enforcing the integral constraint (5), thereby producing two algebraic equations for the x and y components.

2.2. Results and discussion

Fig. 2 presents coded plots of the magnitude of the tangential component of the boundary traction representing the shear stress for flow along the x axis. The boundary elements for an intermediate discretization involving 144 elements are also shown in the four panels. Each computation at this discretization consumes approximately 15 min of CPU time on a high-end workstation. Red color represents high shear stress and blue color represents low shear stress.

The results confirm that the flow decays rapidly with downward distance from the tip of each rod. As the radius of the rods decreases or the rod separation increases, the flow is able to penetrate deeper into the array. We found that, for the boundary element discretization implemented, the assumption of a semi-infinite array is valid approximately for $a/L > 0.1$. For larger separations or smaller tube radii, the shear flow is able to reach the bottom of the truncated cylinders. In the experiments of Ni et al. (2008), nanotubes with radius $a \sim 20-30$ nm and spacing $L \simeq 200$ nm were synthesized using a thermal chemical vapor deposition technique, corresponding to scaled nanotube radius $a/L \sim 0.10-0.15$. Our computations are marginally able to describe flow over this moderately populated array in the absence of a substrate.

Figs. 3(*a, b*) shows the x component of the slip velocity plotted against the cylinder radius scaled by the cylinder separation, a/L, for flow along the x axis over a square or hexagonal array. The maximum possible value, $a/L = 0.5$, corresponds to touching cylinders. The diamonds, squares, and circles represent results obtained with 36, 144, and 576 boundary elements. The numerical predictions converge linearly with respect to the number of boundary elements. The

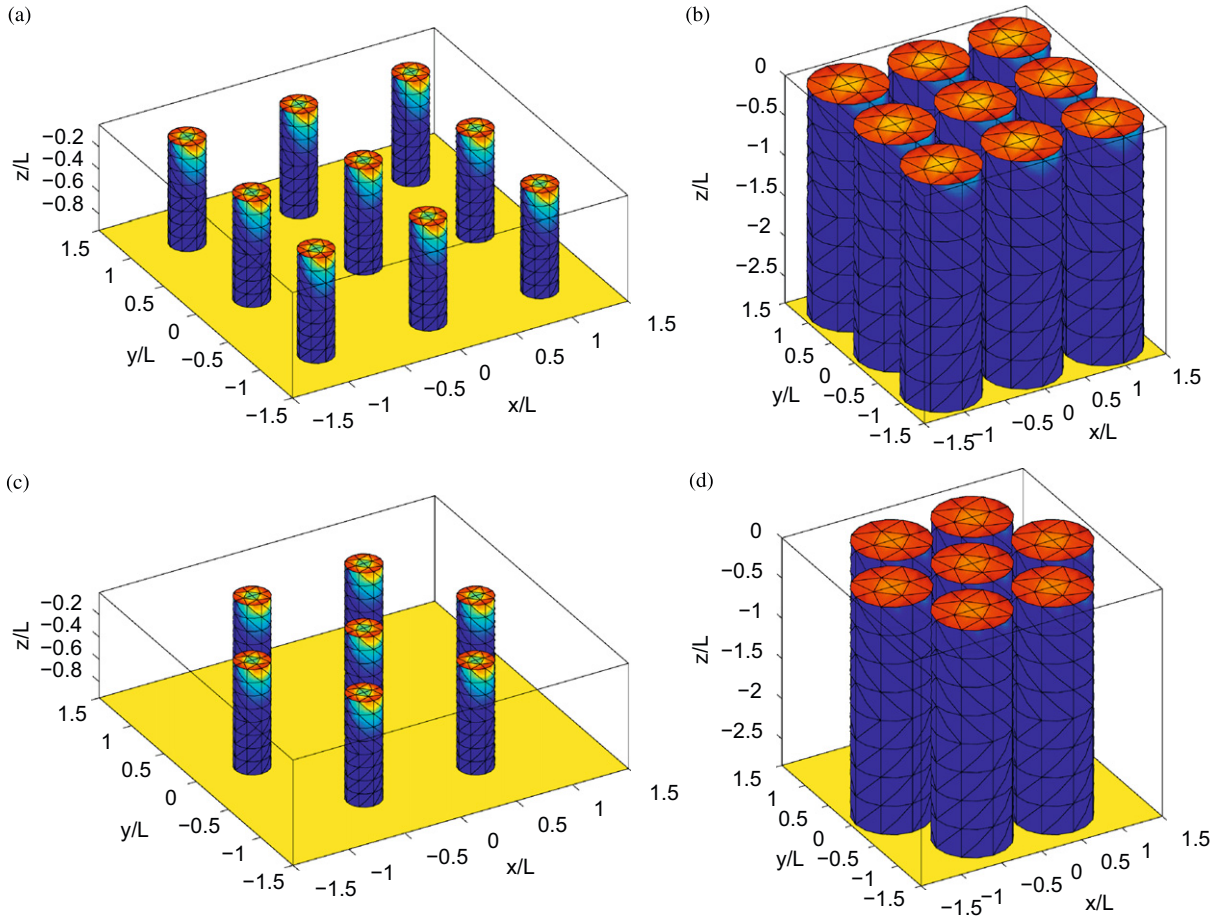

Fig. 2. Color coded plots (in electronic version) of the magnitude of shear stress for a square nanotube array with scaled tube radius (a) $a/L = 0.15$, and (b) 0.45. (c, d) Same as (a, b) but for a hexagonal array. Red color represents high shear stress and blue color represents low shear stress. (For interpretation of the references to color in this figure legend, the reader is referred to the web version of this article.)

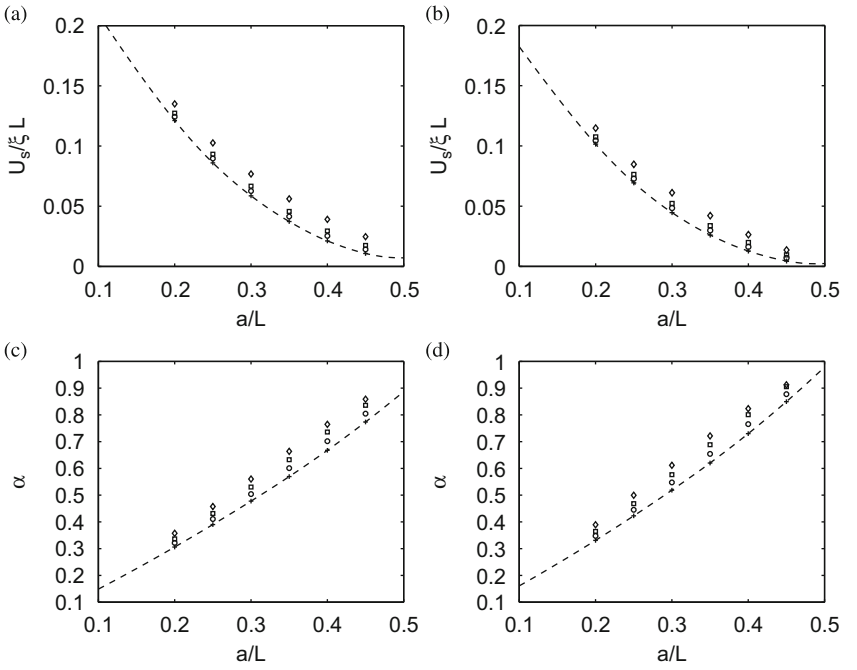

Fig. 3. (a, b) Graphs of the slip velocity for flow along the x axis, plotted against the scaled cylinder radius, a/L, for (a) a square and (b) a hexagonal array. (c, d) Percentage of x component of the force imparted to the top surface (cap) of each tube for (c) a square and (d) a hexagonal array. The diamonds, squares, and circles represent results obtained with 36, 144, and 576 boundary elements. The crosses extrapolate the results to the limit of vanishing numerical discretization error.

crosses extrapolate the results to the limit of infinite resolution by Richardson extrapolation. The dashed lines interpolate and extrapolate the extrapolated data using piecewise cubic Hermite interpolation. We observe that the slip velocity is only mildly sensitive to the lattice type. For both lattice types considered, as a/L increases toward the maximum value of 0.5, the slip velocity decreases and tends to a well-defined limit. As a/L tends to zero, the slip velocity diverges due to the inability of the needle-like rods to sustain the shear flow in the absence of a support.

The results reveal that the hydrodynamic traction in dense arrangements is concentrated near the top surface of the nanotubes due to hydrodynamic screening, as illustrated in Fig. 2. Figs. 3(c,d) shows a graph of the fraction of the x component of the force exerted by the shear flow at the top surface (cap) of each tube, α, for the square and hexagonal array. In the case of densely populated nanotubes, $a/L > 0.45$, more than 80% of the force is exerted on the top surface.

Nanotubes bend under the influence of the stress imparted to them by the simple shear flow. Ni et al. (2008) demonstrated that the nanotube deformation can be used to infer the flexural stiffness, as discussed in the Introduction. Once this is known, the nanotube deformation can be calibrated to produce the surface shear stress. Ni et al. (2008) modeled the nanotubes as cantilever beams that are fixed at the lower end on the substrate and are free to deform at the exposed end. A distributed side load was applied according to a local drag coefficient that depends on the local fluid velocity using the Stokes–Oseen formula for flow past an infinite cylinder.

In a simplified model, the deformation of each nanotube can be estimated by assuming that the hydrodynamic load is concentrated at the tip of a cantilever. Elementary analysis shows that the beam deflection is described by the simplified formula

$$f(x) \simeq \mu\xi A \frac{d^3}{6EI}\left(1-\frac{x}{d}\right)^2\left(2+\frac{x}{d}\right), \tag{6}$$

where A is the area of a unit cell in the xy plane, d is the length of the cantilever, E is the elastic modules, I is the cross-sectional moment of inertia, and the product EI is the flexural rigidity. The origin of the x axis is set at the far end of the cantilever. The maximum displacement occurs at the tip located at $x = 0$. The cubic dependence of the maximum deflection on d is consistent with results shown in Fig. 4(a) of Ni et al. (2008). Given all geometrical and physical parameters, A, d, E, I, and a pointwise deflection, expression (6) can be used to estimate the wall shear stress, $\mu\xi$.

In the experiments of Ni et al. (2008), a nanomat was inserted in a quartz tube with inner diameter 6.2 mm, and air was supplied with average velocity $U \simeq 40$ m/s. According to the Blasius boundary-layer solution for flow past a

semi-infinite plate, the wall shear stress is

$$\tau \equiv \mu\xi \simeq 0.332 U^{3/2} \left(\frac{\mu\rho}{x}\right)^{1/2}, \tag{7}$$

where ρ is the density of air and x is the distance from the leading edge. Substituting $\rho = 1.2\,\mathrm{kg/m^3}$ and $\mu = 1.73 \times 10^{-5}\,\mathrm{Ns/m^2}$ for the density and viscosity of air, we find $\tau \simeq 3.8 \times 10^5/\sqrt{x}$ in units of $\mathrm{N/m^2}$, where the distance x is measured in μm. For nanotube length $d = 40\,\mu\mathrm{m}$, the maximum deflection was observed to be approximately $f(0) \simeq 1.5\,\mu\mathrm{m}$. Since the nanotubes were separated approximately by distance $L \simeq 200\,\mathrm{nm}$, we set $A \simeq L^2 \simeq 10^{-13}\,\mathrm{m^2}$ for the surface area of each unit cell and obtain an estimate for the flexural stiffness,

$$EI \simeq \frac{\tau A d^3}{3f(0)} \simeq \frac{5.4}{\sqrt{x}} \times 10^{-16}\,\mathrm{Nm^2}. \tag{8}$$

For $x \simeq 100\,\mu\mathrm{m}$, this estimate is consistent with the value $8.8 \times 10^{-16}\,\mathrm{Nm^2}$ inferred by Ni et al. (2008) based on a more elaborate theoretical model.

3. Small deformation of an elastic rod

In the second part of this work, we consider shear flow past an isolated cylindrical rod with length d and radius a attached to an infinite plane, as shown in Fig. 4(*a*). Far from the rod, the velocity field describes simple shear flow along the y axis with velocity components $u_x^\infty = 0$, $u_y^\infty = \xi y$, $u_z^\infty = 0$, where ξ is the shear rate. The labeling of the Cartesian axes with the x axis perpendicular to the plane wall and the y and z axes parallel to the plane wall is motivated by the Fourier decomposition with respect to the meridional angle, φ, discussed next. Our objective is to describe the small flow-induced deflection from the perfectly straight shape taking into consideration the precise distribution of the hydrodynamic load.

3.1. Boundary-integral formulation

The velocity at a point in the flow past the undeflected rod can be produced by linearly superposing the unperturbed shear flow and three single-layer Stokes flow potentials defined over the exposed rod surface (R), discoidal rod base attached to the wall (B), and wall surface outside the base of the rod (W),

$$\mathbf{u}(\mathbf{x}) = \mathbf{u}^\infty - \mathbf{l}^s(\mathbf{x},\mathbf{f},R) - \mathbf{l}^s(\mathbf{x},\mathbf{f}^D,W) + \mathbf{l}^s(\mathbf{x},\mathbf{f}^\infty,B), \tag{9}$$

where $\mathbf{f} = \mathbf{n} \cdot \boldsymbol{\sigma}$ is the hydrodynamic traction, $\boldsymbol{\sigma}$ is the stress tensor, $\mathbf{n}$ is the unit vector normal to the boundaries pointing into the flow over R and W and into the upper half space over B, and the superscript D denotes the disturbance flow

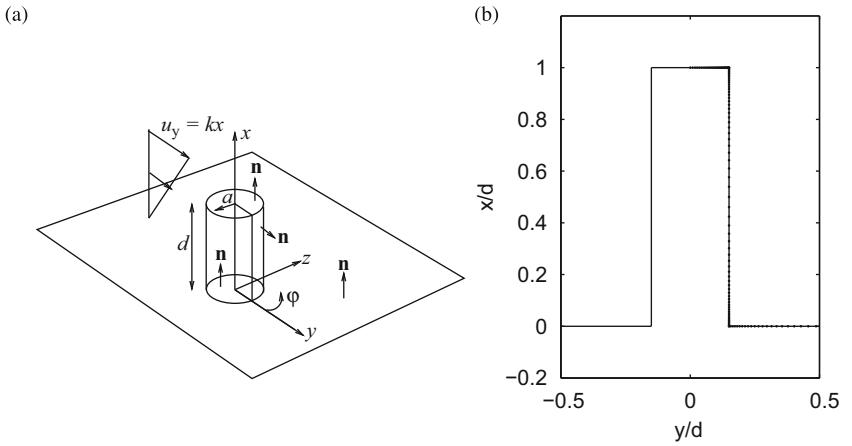

Fig. 4. (a) Schematic illustration of shear flow past a cylindrical with length d and radius a attached to an infinite plane. (b) Typical boundary-element discretization of the rod and wall contour in the $\varphi = 0$ meridional plane.

(Pozrikidis, 1997). We have introduced the single-layer potential of Stokes flow defined over a surface Ω,

$$\mathbf{I}^s(\mathbf{x},\mathbf{f},\Omega) \equiv \frac{1}{8\pi\mu}\iint_{\Omega} \mathbf{G}(\mathbf{x}-\mathbf{x}')\cdot\mathbf{f}\,\mathrm{d}S(\mathbf{x}'), \tag{10}$$

where

$$\mathbf{G}(\mathbf{x}) = \frac{\mathbf{I}}{|\mathbf{x}|} + \frac{\mathbf{x}\mathbf{x}}{|\mathbf{x}|^3} \tag{11}$$

is the free-space Green's function, and $\mathbf{I}$ is the identity matrix.

In the particular case of simple shear flow along the y axis, the cylindrical polar components of the velocity exhibit harmonic dependencies on the meridional angle, φ, in the form

$$u_x = \xi\, dU_x(x,\sigma)\cos\varphi, \quad u_\sigma = \xi\, dU_\sigma(x,\sigma)\cos\varphi, \quad u_\varphi = -\xi\, dU_\varphi(x,\sigma)\sin\varphi, \tag{12}$$

where U_x, U_σ, and U_φ are three dimensionless functions. The unperturbed simple shear flow is described by $U_x = 0$, $U_\sigma = x/d$, and $U_\varphi = x/d$. Motivated by the linearity of the governing equations, we express the cylindrical polar components of the traction in the corresponding form

$$f_x = \mu\xi\mathcal{F}_x(x,\sigma)\cos\varphi, \quad f_\sigma = \mu\xi\mathcal{F}_\sigma(x,\sigma)\cos\varphi, \quad f_\varphi = -\mu\xi\mathcal{F}_\varphi(x,\sigma)\sin\varphi. \tag{13}$$

The Fourier coefficients of the simple shear flow over the base are given by $\mathcal{F}_x = 0$, $\mathcal{F}_\sigma = 1$, and $\mathcal{F}_\varphi = 1$. Substituting (12) and (13) in (9) and performing the integration in the meridional direction we derive integral representations for the cylindrical polar components of the velocity over the trace of the boundaries in the $\varphi = 0$ meridional plane. Now taking the limit as the point $\mathbf{x}$ approaches the flow boundaries, we derive three one-dimensional linear integral equations for the dimensionless coefficient $\mathcal{F}_\alpha$. The solution was found using a standard boundary-element method. A typical boundary-element discretization in a meridional plane is shown in Fig. 4(*b*). Note that the boundary elements are highly concentrated near the corners to resolve the fine features of the flow.

The y component of the force and z component of the torque with respect to a point $\mathbf{x}_0 = (x_0,0,0)$ exerted on the rod can be expressed as line integrals with respect to arc length l measured along the trace of the rod in the $\varphi = 0$ meridional plane,

$$F_y = \pi\mu\xi d\int \Phi(l)\,\mathrm{d}l, \quad T_z = \pi\mu\xi\, d^2\int \Psi(l)\,\mathrm{d}l, \tag{14}$$

where

$$\Phi = (\mathcal{F}_\sigma + \mathcal{F}_\varphi)\frac{\sigma}{d}, \quad \Psi = ((x-x_0)(\mathcal{F}_\sigma + \mathcal{F}_\varphi) - \sigma\mathcal{F}_x)\frac{\sigma}{d^2} \tag{15}$$

are dimensionless functions.

3.2. Rod deflection

After the boundary traction has been computed, the beam centerline deflection described by the function $y = f(x)$ is computed by solving the Euler–Bernoulli equation

$$EI\frac{\mathrm{d}^4 f}{\mathrm{d}x^4} = w(x), \tag{16}$$

where E is an elastic modulus of the beam material with units of stress, $I = \frac{1}{4}\pi a^4$ is the second areal moment of inertia of the rod cross-section, and $w(x)$ is the linear density of a distributed hydrodynamic load with units of force divided by length. Referring to the first equation in (14), we set $w(x) = \pi\mu\xi\,\mathrm{d}\Phi(x)$. The boundary conditions specify

$$f(0) = 0, \quad \frac{\mathrm{d}f}{\mathrm{d}x} = 0, \quad EI\left(\frac{\mathrm{d}^3 f}{\mathrm{d}x^3}\right)_{x=d} = F_y^{\mathrm{top}}, \quad EI\left(\frac{\mathrm{d}^2 f}{\mathrm{d}x^2}\right)_{x=d} = T_z^{\mathrm{top}}, \tag{17}$$

where F_y^{top} and T_z^{top} are the force and torque exerted on the discoidal top surface of the rod. The Euler–Bernoulli equation was solved by a standard finite-element method employing Hermitian elements (Pozrikidis, 2005).

3.3. Results and discussion

Fig. 5(*a*) shows the distribution of shear stress along the contour of the top of the rod, the side surface of the rod, and the plane wall in the xy plane. The origin of arc length, s, has been set at the top rim corner point. Results are shown for a sequence of radius to height ratios, a/d. As the rod becomes increasingly slender, $a/d \to 0$, the shear stress

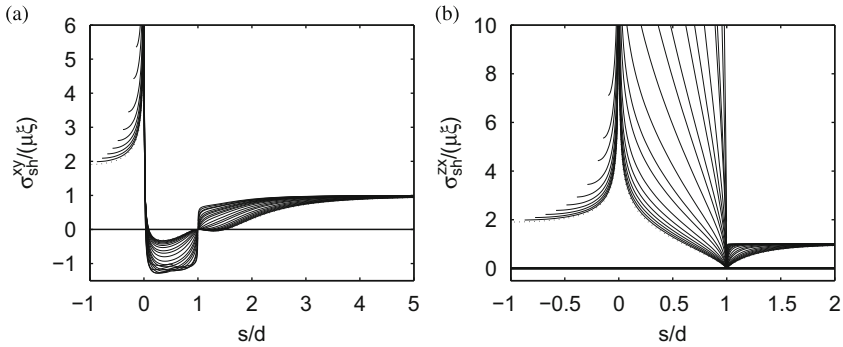

Fig. 5. (a, b) Shear stress distribution along the contour of the cylinder and wall in the xy and zx plane, plotted against the arc length s, for cylinder aspect ratio $a/d = 0.001$, 0.002, 0.004, 0.005, 0.010, 0.015, 0.02, 0.03, 0.04, 0.06, 0.10, 0.15, 0.20, 0.30, …, 1.0 (dotted line). The origin of arc length, $s = 0$, has been set at the upper circular rim.

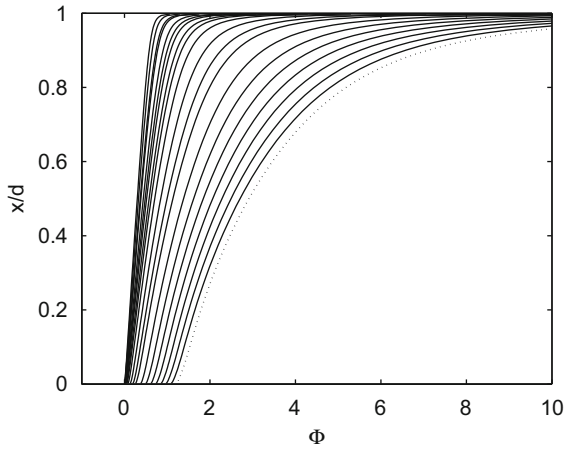

Fig. 6. Distribution of the load function Φ along the cylinder length for cylinder aspect ratio $a/d = 0.001$, 0.002, 0.004, 0.005, 0.010, 0.015 0.02, 0.03, 0.04, 0.06, 0.10, 0.15, 0.20, 0.30, …, and 1.0 (dotted line).

monotonically increases over the top. An expected discontinuity due to the corner flow occurs at the top circular rim. As we move downward from the top to the bottom along the side surface, the shear stress decreases, takes negative values indicating the onset of recirculating flow, and then vanishes around the bottom corner point. Fig. 5(*b*) shows the corresponding distribution of the shear stress along the contour of the cylinder and wall in the zx plane. This shear stress is positive along the whole boundary contour.

Fig. 6 shows the distribution of the dimensionless function $\Phi(x)$ defined in (15), describing the distributed streamwise hydrodynamic load exerted on an infinitesimal cross-section. Results are shown for a sequence of rod radius to height ratios, a/d, corresponding to those presented in Fig. 5. As we approach the top of the rod along the centerline, the hydrodynamic load increases monotonically and exhibits an integrable singularity due to the sharp corner around the rim of the discoidal cap. As the rod radius decreases, the distribution of the load becomes less gradual.

Figs. 7(a, b) shows graphs of the y component of the force exerted on the rod (solid lines) and z component of the torque with respect to the origin of the Cartesian axes located at the infinite plane (broken lines). The circles and diamonds in Fig. 7(b) represent results of computations using a boundary-element method discussed in Section 4. As the cylinder radius becomes larger, the force and torque increase approximately at a constant rate. As the cylinder radius becomes smaller, the force and torque both tend to zero. The behavior for small radii can be described using slender-body theory predicting that, in the limit of zero radius, the force and torque scale with the inverse of the log of the aspect ratio, $1/\ln(d/a)$ (Batchelor, 1970). Fitting our numerical results to this functional form, we obtain

$$F_y \simeq \mu\xi d^2 \frac{2.18}{\ln(d/a)}, \quad T_z \simeq \mu\xi d^3 \frac{1.47}{\ln(d/a)}, \tag{18}$$

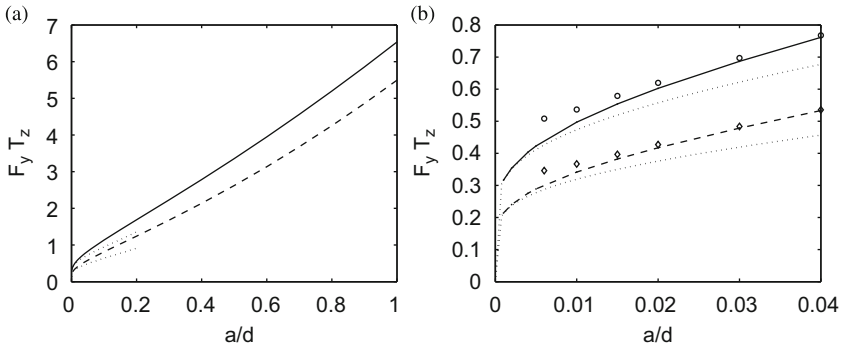

Fig. 7. Graphs of (a) the y component of the force exerted on the cylinder scaled by $\pi\mu\xi d^2$ (solid line), and z component of the torque with respect to the origin of the Cartesian axes scaled by $\pi\mu\xi d^3$ (dashed line). (b) Magnification of the graphs for small radii to show agreement with slender-body theory represented by the dotted lines. The circles and diamonds represent the results of a boundary-element method discussed in Section 4. The dotted lines represent the predictions of slender-body theory.

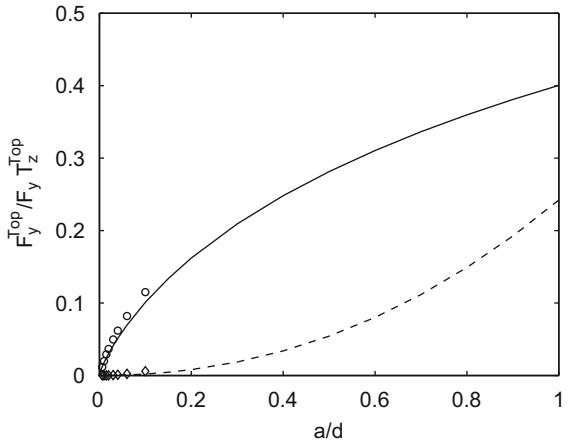

Fig. 8. The solid line represents that ratio of the y component of the force exerted on the top of the cylinder reduced by the total y component of the force exerted on the cylinder. The broken line represents the z component of the torque exerted on the top of the cylinder with respect to the top centerpoint of the cylinder, scaled by $\pi\mu\xi d^3$. The circles and diamonds represent the results of a boundary-element method discussed in Section 4.

represented by the dotted lines in Figs. 7(a, b). A sharp decline in the force and torque occurs approximately when $a/d < 10^{-3}$.

The solid line in Fig. 8 shows a graph of the ratio of the y component of the force exerted on the top of the cylinder to the y component of the total force exerted on the whole cylinder surface. The broken line shows a graph of the scaled z component of the torque exerted on the top of the cylinder with respect to the top centerpoint, $(d,0,0)$. The circles and diamonds represent the results of a boundary-element method discussed in Section 4. As the cylinder becomes increasingly slender, the ratio of the top to the total force tends to zero with a finite slope. In contrast, the torque tends to zero with zero slope and curvature, and the magnitude of the torque is negligible even for moderate rod radii.

Fig. 9 shows deformed centerline profiles for a sequence of rod aspect ratios computed by the finite-element method. All profiles have been scaled by the maximum deflection of a cantilever subject to a concentrated end-load, given by $f_0 \equiv F_y d^3/(3EI)$, where F_y is the total force exerted on the rod. The results show that the rod deflection arising from the finite-element solution is less severe than that of a cantilever with a concentrated load (dashed line), but more pronounced than that of a cantilever with a uniform load (dot-dashed line). As the rod becomes increasingly slender, the profiles uniformly converge to a limiting shape for a fiber, exhibiting a transition from a concentrated-load shape to a uniform-load shape. The profiles shown in Fig. 9 in conjunction with the data shown in Fig. 7 can be used to estimate the flexural rigidity, EI, based on photographs of the deformation of an attached rod.

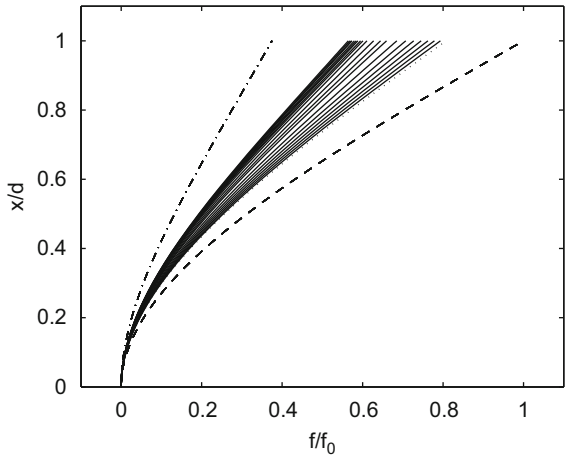

Fig. 9. Deformed rod profiles for aspect ratio $a/d = 0.001$ (leftmost solid line), 0.002, 0.004, 0.005, 0.010, 0.015 0.02, 0.03, 0.04, 0.06, 0.10, 0.15, 0.20, 0.30, …, 1.0 (dotted line). The dashed line traces the cubic profile of a deformed cantilever subject to a concentrated end load that is equal to the total force exerted on the rod. The dot-dashed line traces the cubic profile of a deformed cantilever subject to a distributed uniform load whose integral amounts to the total force exerted on the rod.

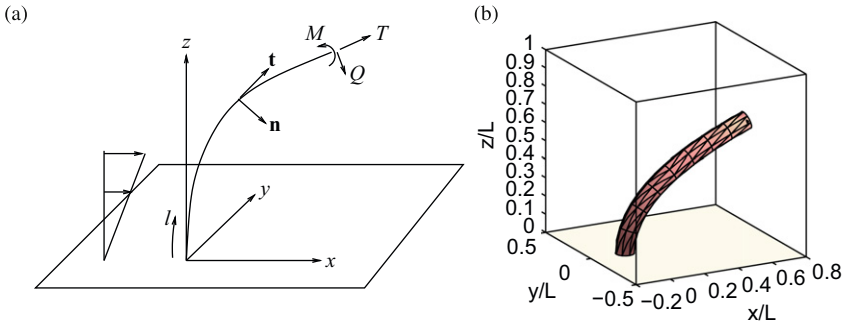

Fig. 10. (a) Schematic depiction of a rod deflecting due to an incident simple shear flow. (b) Boundary-element discretization of the top and side surface of a rod with radius to length ratio $a/d = 0.05$, respectively, into 16 and 128 elements.

4. Large deformation of a flexible rod

In the third part of this paper, we consider shear flow past a significantly deflected cylindrical rod of length d and radius a attached to an infinite plane located at $z = 0$, as illustrated in Fig. 10(a). The labeling of the Cartesian axes is consistent with those introduced in Section 2. Far from the rod, the velocity field describes simple shear flow along the x axis with velocity components $u_x^\infty = \xi z$, $u_y^\infty = 0$, $u_z^\infty = 0$, where ξ is the shear rate. Our objective is to describe steady deflected rod shapes relaxing the assumption of small deformation invoked in Section 3.

4.1. Hydrodynamics

The velocity at a point in the flow, $\mathbf{x}_0$, is given by the integral representation

$$\mathbf{u}(\mathbf{x}_0) = \mathbf{u}^\infty(\mathbf{x}_0) - \mathbf{I}^s(\mathbf{x}_0, \mathbf{f}, R), \tag{19}$$

where $\mathbf{I}^s$ is the single-layer potential defined in (12) supported by the rod side and top surface, R. The kernel $\mathbf{G}$ of the single-layer potential is the Green's function of Stokes flow for a semi-infinite domain bounded by a plane wall [e.g.,

Pozrikidis (1992)]. Enforcing the integral representation at the surface of the rod and requiring the condition of zero velocity provides us with an integral equation for the hydrodynamic traction.

To solve the integral equation, we divide the top and side surface of the rod into six-node flat or curved boundary elements, as illustrated in Fig. 10(b). The side surface arises by rolling a discretized square into a cylinder of radius a and length $2\pi a$, and then stretching the cylinder to achieve a desired length, d. Approximating the Cartesian components of the traction with constant functions over each element and enforcing the integral equation at collocation points located at the boundary element centroids, we obtain a system of linear algebraic equations for the Cartesian components of the element traction. To demonstrate the accuracy of the method, in Figs. 7(b) and 8 we indicate with circles and diamonds results for a straight rod discretized into 16 elements over the top and 128 elements over the side surface of the rod, as shown in Fig. 10(b). Considering the modest number of boundary elements employed, the accuracy of the numerical results is remarkable for aspect ratios as small as $a/d \simeq 0.01$.

4.2. Beam approximation and rod reconstruction

In the limit of high aspect ratio, the rod reduces into a slender beam described by the centerline profile, $\mathbf{x} = \boldsymbol{\mathcal{F}}(l)$, where l is the arc length along the centerline measured from the point of attachment, varying in the interval $[0,d]$. The beam deflection from the vertical shape is defined as $\delta\mathbf{x}(l) = \boldsymbol{\mathcal{F}}(l) - \boldsymbol{\mathcal{F}}_0(l)$, where the subscript 0 denotes the undeformed straight profile. In the numerical implementation, the discretized top and side surfaces of the rod are reconstructed from the centerline profile in three stages. First, the surface of a perfectly straight cylindrical rod with length d and radius a is discretized into boundary elements defined by element nodes. Second, the z coordinate of each node serves as an interpolation variable for displacing the points by $\delta\mathbf{x}(z)$, where $0 \le z \le d$. Third, the position of each element node is rotated around the y axis about the displaced centerline point located at $\boldsymbol{\mathcal{F}}(z)$ according to the derivative $\mathrm{d}\boldsymbol{\mathcal{F}}/\mathrm{d}l$, so that each cross-section of the rod remains perpendicular to the centerline in the deformed configuration. Collocation points are then defined at the element centroids and the integral equation is solved.

4.3. Beam deflection formulation

Because of the distributed side and tip load, the beam representing the backbone of the rod develops a tangential in-line force, T, a transverse shear force in the zx plane, Q, and a bending moment about the y axis, M, as illustrated in Fig. 10(a). The vectorial force exerted on a beam cross-section is $\mathbf{F} = T\mathbf{t} + Q\mathbf{n}$, where $\mathbf{t}$ is the unit tangent vector pointing in the direction of increasing arc length, l, and $\mathbf{n}$ is the unit normal vector. A differential force balance over an infinitesimal section requires the equilibrium condition

$$\frac{\mathrm{d}\mathbf{F}}{\mathrm{d}l} + \mathbf{p} = \frac{\mathrm{d}}{\mathrm{d}l}(T\mathbf{t} + Q\mathbf{n}) + \mathbf{p} = \mathbf{0}, \tag{20}$$

where $\mathbf{p}$ is a distributed load. Expanding the derivatives of the products on the left-hand side and using the Frenet relations $\mathrm{d}\mathbf{t}/\mathrm{d}l = -\kappa\mathbf{n}$ and $\mathrm{d}\mathbf{n}/\mathrm{d}l = \kappa\mathbf{t}$, we obtain the normal and tangential force balances

$$-\kappa T + \frac{\mathrm{d}Q}{\mathrm{d}l} = -\mathbf{p}\cdot\mathbf{n} \equiv -p_n, \quad \kappa Q + \frac{\mathrm{d}T}{\mathrm{d}l} = -\mathbf{p}\cdot\mathbf{t} \equiv -p_t, \tag{21}$$

where κ is the beam curvature of the in the zx plane. Performing a torque balance over an infinitesimal cross-section, we find $Q = \mathrm{d}M/\mathrm{d}l$. Next, we introduce a linear constitutive equation for the bending moments expressed by the relation $M = E_B\kappa$, where $E_B = EI$ is a bending modulus with dimensions of force multiplied by length. Rearranging the preceding equations we derive a nonlinear coupled system,

$$\frac{\mathrm{d}T}{\mathrm{d}l} = -\kappa Q - p_t, \quad \frac{\mathrm{d}Q}{\mathrm{d}l} = \kappa T - p_n, \quad \frac{\mathrm{d}\kappa}{\mathrm{d}l} = \frac{Q}{E_B}. \tag{22}$$

At the far end of the beam, $l = d$, we specify T, Q, and the curvature κ according to M. The corresponding attachment-point values, $T(0)$, $Q(0)$, and $\kappa(0)$, must be found as part of the solution.

To compute the shape of the deformed beam in terms of the curvature in the zx plane, $\kappa(l)$, we regard the x and y coordinates of material point particles distributed along the centerline as functions of arc length in the deformed configuration, l, writing $x = x_1(l)$ and $y = x_2(l)$. By definition then, $x_1'^2 + x_2'^2 = 1$, where a prime denotes a derivative with respect to l. Using elementary differential geometry, we derive the relations

$$\kappa = -x_1''x_2' + x_1'x_2'' = -\frac{x_1''}{x_2'} = \frac{x_2''}{x_1'}. \tag{23}$$

Next, we introduce the derivative functions $x_3 \equiv x'$ and $x_4 \equiv y'$, and obtain the following system of four nonlinear differential equations,

$$\frac{dx_1}{dl} = x_3, \quad \frac{dx_2}{dl} = x_4, \quad \frac{dx_3}{dl} = -\kappa x_4, \quad \frac{dx_4}{dl} = \kappa x_3. \tag{24}$$

Given the distributed load, $\mathbf{p}(l)$, the deformed beam shape is governed by a system of seven first-order ordinary differential equations for T, Q, κ, x_1, x_2, x_3, and x_4, comprised of Eqs. (22) and (24). Putting the origin of the Cartesian axes at the point of attachment and fixing the slope, we obtain four initial conditions,

$$x_1(0) = 0, \quad x_2(0) = 0, \quad x_3(0) = 0, \quad x_4(0) = 1. \tag{25}$$

The solution of the boundary-value problem was found using the internal matlab function `bvp4c`.

To convert the hydrodynamic traction exerted on the rod surface into beam load, we work as follows. Given a rod shape, the boundary-element tractions are computed by solving the integral equation discussed earlier in the section, and are then multiplied by the element surface areas to give element forces. The forces on elements on the side of the cylinder are transferred as pointwise loads to the beam centerline and then smoothed to give a discontinuous distributed load, $\mathbf{p}$. The forces on elements on the top of the cylinder yield a tip force, $\mathbf{F}_d$, accompanied by a moment with respect to the end of the centerline, M_d.

The equilibrium beam shape is found by iteration. A beam shape is assumed, the rod shape is reconstructed, the boundary-element traction is computed, the beam load is calculated, a new beam shape is obtained, and the process is repeated until convergence. Since the boundary-element code was written in fortran and the boundary-value problem was solved in matlab, the iterations are carried out by recording and reading output and input data files. Only a few iterations are necessary for the results to converge with tolerance comparable to the numerical discretization error.

4.4. Results and discussion

The rod deflection is determined by the dimensionless bending stiffness, $\hat{E}_B \equiv E_B/(\xi d^3)$. Fig. 11 shows a family of deflected beam centerline profiles for rod aspect ratio $a/d = 0.05$. A three-dimensional shape of a deflected rod for $\hat{E}_B = 0.3$ is shown in Fig. 10(b). The results are in agreement with physical intuition: as the bending stiffness is reduced or the shear rate increases, the rod exhibits a predominantly horizontal deflection and then inclines to accommodate the shear flow. The tip of the rod tends to become horizontal at high shear rates. The dotted lines in Fig. 11 represent the predictions of the small-deformation theory discussed in Section 3. Apart from not conserving the specified length of the rod, the small-deformation analysis is remarkably accurate even for moderate deformations and can be used to accurately deduce the bending stiffness from laboratory observation.

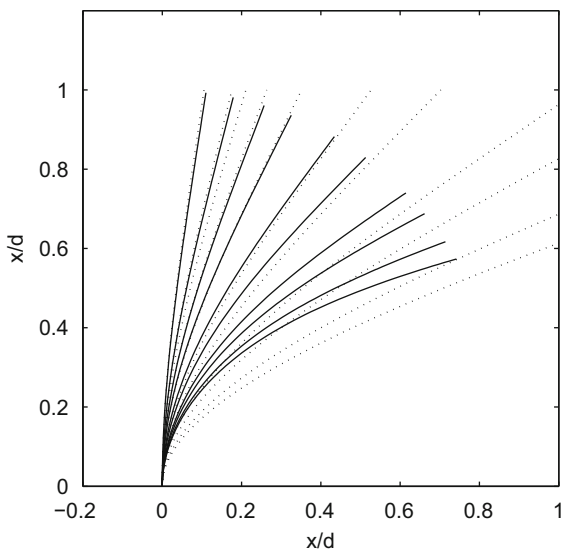

Fig. 11. Deflected rod centerline profiles for rod aspect ratio $a/d = 0.05$ and dimensionless bending stiffness $\hat{E}_B \equiv E_B/(\xi d^3) = 5, 3, 2, 1.5, 1.0, 0.75, 0.5, 0.4, 0.3, 0.25$. The dotted lines represent the predictions of the small-deformation theory.

5. Summary and discussion

We have discussed shear flow over a surface hosting an array of cylindrical rods with applications to flow over a carbon nanomat consisting of nanotubes and presented numerical results on the macroscopic slip velocity. A boundary-element analysis employing the doubly periodic Green's function provided us with data for the concentrated hydrodynamic load applied at element centroids over the top and side surface of the rods. Due to hydrodynamic shielding, most of the load is exerted near the exposed tips of the periodic array. In light of the slenderness of the nanotubes, bending can be described by the Euler–Bernoulli theory for a elongated beams, and accurate predictions for the nanotube deformation can be obtained.

We have computed the deflection of an isolated rod attached to a flat substrate under the action of a shear flow for small and large deformation. In the case of flow past a slightly deformed rod, the surface traction was computed with high accuracy by introducing a Fourier expansions and solving one-dimensional integral equations. In the case of flow past a significantly deformed rod, deflected shapes were computed by iteration using a boundary-element method and accurate numerical results on beam deflection were obtained by iteration. The accuracy of the small-deflection theory was confirmed well into the regime of moderate deformation.

This work was motivated by the hydrodynamics of shear flow over a nanomat consisting of attached carbon nanotubes. A precise description of the force and torque exerted on a rod attached to a plane is of interest in biophysics with reference to the function of the stereocilia. Flow over a surface populated by nanotubes is similar to flow over a ciliated substrate. In biological applications, the synchronized active beating of cilia drives a flow that may feed a microorganism or transport fluid. In contrast, at the present time, nanotubes deployed over a nanomat exhibit only passive, fluid-induced deformation.

Acknowledgment

This research was supported by a grant provided by the National Science Foundation.

References

Batchelor, G.K., 1970. Slender-body theory for particles of arbitrary cross-section in Stokes flow. Journal of Fluid Mechanics 44, 419–440.

Deck, C.P., Vecchio, K., 2005. Growth mechanism of vapor phase CVD-grown multi-walled carbon nanotubes. Carbon 43, 2608–2617.

Ford, A.N., Papavassiliou, D.V., 2006. Flow around surface attached carbon nanotubes. Industrial & Engineering Chemistry Research 45, 1797–1804.

Pozrikidis, C., 1992. Boundary Integral and Singularity Methods for Linearized Stokes Flow. Cambridge University Press, New York.

Pozrikidis, C., 1996. Computation of periodic Green's functions of Stokes flow. Journal of Engineering Mathematics 30, 79–96.

Pozrikidis, C., 1997. Shear flow over a protuberance on a plane wall. Journal of Engineering Mathematics 31, 29–42.

Pozrikidis, C., 2001. Shear flow over a particulate or fibrous plate. Journal of Engineering Mathematics 39, 3–24.

Pozrikidis, C., 2005. Introduction to Finite and Spectral Element Methods Using Matlab. Chapman & Hall/CRC Press, Boca Raton.

Ni, C., Deck, C., Vecchio, K.S., Bandaru, P.R., 2008. Optical determination of the flexural rigidity of carbon nanotube ensembles. Applied Physics Letters 92, 173106.

Xu, Y.-Q., Flor, E., Kim, M.J., Hamadani, B., Schmidt, H., Smalley, E.E., Hauge, R.H., 2006. Vertical array growth of small diameter single-walled carbon nanotubes. Journal of the American Chemical Society 128, 6560–6561.